Catalysis Letters
https://doi.org/10.1007/s10562-024-04640-y

# The Effect of Reduction Pretreatments on the Size of Supported Pt and Pd Nanoparticles Prepared by Strong Electrostatic Adsorption

**Md. Fakhruddin Patwary[1] · Manuel Neito[2] · Alaba Ojo[1] · John R. Regalbuto[1]**

Received: 17 October 2023 / Accepted: 24 February 2024


## Abstract

Supported catalyst synthesis involves pretreatment (drying, reduction) of metal complexes to form metal nanoparticles. This study has been undertaken to explore the effect of reduction temperature, heating rate, and water partial pressure on final particle size of Pt and Pd supported on a total of four carbon and oxide supports. Supported nanoparticles were synthesized by strong electrostatic adsorption (SEA) and dry impregnation (DI); the former method was hypothesized to yield greater nanoparticle stability in thermochemical reducing environments stemming from the strong interaction of the precursor with the support during impregnation. Reduced samples were characterized by in-situ and ex-situ XRD and STEM. The DI-derived samples generally showed an expected increase of particle size with increased reduction temperature, and severe particle coalescence in humid hydrogen, while the SEA-derived samples did not sinter at the elevated reduction temperatures (up to 500 °C) and were remarkably stable in the humid reducing environment.

## Graphical Abstract

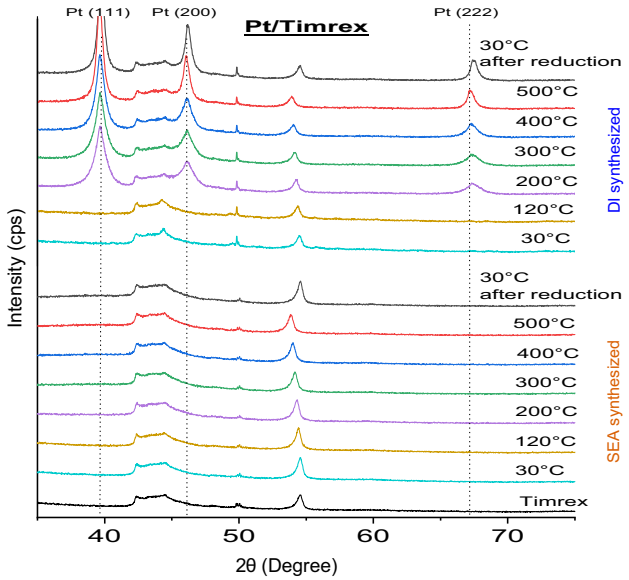


**Keywords** Nanoparticle sintering · Reduction Temperature · Heating rate · Moisture · Strong electrostatic adsorption · Dry impregnation

Extended author information available on the last page of the article

Published online: 17 March 2024

## 1 Introduction

Heterogeneous catalysts are very widely used in chemical processing to provide an inherent separation of reaction products from the catalyst. Typical heterogeneous catalysts consist of transition metal nanoparticles anchored against sintering on an inert, porous, high temperature stable support. As the reaction of a gaseous or liquid phase with a solid metal catalyst can only occur on the metal nanoparticle surface, and noting that transition metals are often quite expensive, the normal desire is to maximize the number of atoms exposed for reaction in the metal particles by synthesizing them to be as small as possible [1]. As a general benchmark, metal particles measuring 1 nm in diameter are considered to be 100% dispersed, that is, to have all of atoms accessible for chemical reaction [2]. If the metal is well dispersed, minimized amounts of the costly metal can provide a requisite level of catalytic activity. For example, Burkholder et.al. [3] showed a 50–55 wt% Ag catalyst contained only 40% more Ag surface sites as compared to a similarly active 12 wt% Ag catalyst, because the Ag particles were more well dispersed in the lower loading sample. Consequently, the 12% Ag catalyst gave the same level of propylene conversion and propylene oxide selectivity under similar reaction condition, as the 50–55% Ag catalyst.

The size of the catalyst particles can be influenced by the preparation method and pretreatment conditions. Most often, aqueous solutions of metal coordination complexes such as Pt hexachloride, $[PtCl_6]^{2-}$, which forms from the dissolution of chloroplatinic acid ($H_2PtCl_6$) or Pd tetraamine, $[(NH_3)_4Pd]^{2+}$, from salts such as $(NH_3)_4PdCl_2$, $(NH_3)_4Pd(OH)_2$, or $(NH_3)_4Pd(NO_3)_2$, are contacted with the porous support. To form catalytically active metal nanoparticles after the metal precursor has been adsorbed or impregnated onto the support, the chloride, ammonia, or other precursor ligands must be removed, and the metal ion reduced to the zero-valent metallic state. This is most typically accomplished by thermochemical treatment of flowing, diluted hydrogen gas passed over the dried catalyst at elevated temperature. In some cases, an intermediate calcination in diluted oxygen or air is employed. These pretreatment conditions can significantly influence the extent of sintering of nanoparticles and ultimately, the final effectiveness of the catalyst [1]. It is the aim of this paper to understand the influence of pretreatment on final particle size as the sintering of nanoparticles prepared by strong electrostatic adsorption (SEA) [4–9] to those prepared by incipient wetness impregnation or dry impregnation (DI) [10, 11]. The former method invokes a strong interaction of metal coordination complexes with the support surface during the adsorption step. The central hypothesis is that metal precursors deposited by strong electrostatic adsorption, having strong initial interaction with the support, will sinter less than DI-deposited precursors at the same pretreatment conditions.

Several reports have directly studied the effect of thermochemical pretreatments on metal nanoparticle size [12–17]. Kim et. al. reported a decrease in particle size in a Pt-Au bimetallic catalyst with increasing $H_2$ flow and increasing particle size with increasing calcination temperature [12]. One wt% Pd/SBA-15 catalyst was prepared by incipient wetness impregnation and then heated in air, $H_2$, $N_2$ or vacuum at 350 °C for 2 h. Subsequently reduced in $H_2$ flow at 350 °C for 2 h. Vacuum pretreated sample produced the smallest particle size (1.3 nm) whereas $N_2$ pretreated sample gave the largest particle size (10.3 nm) [13]. Loosdrecht et. al. investigated the influence of heating rate and the air-space velocity during calcination on Co/γ-alumina catalyst for Fischer–Tropsch synthesis. They observed increasing the air-space velocity during calcination resulted in better dispersion of metal. Also, increasing the heating rate higher than 1 °C/min resulted in a significant decrease in the catalytic activity [15]. In a recent review, Gao et. al. looked into the effect of pretreatment with oxidative, inert, and reductive gases on supported Ni nanoparticles and stated the need for further research on temperature, dwelling time, and heating rate [14].

Accordingly in this study we present a comprehensive survey of SEA- and DI-prepared Pt and Pd particle sizes over silica, alumina, and carbon supports resulting from the following reducing pretreatments:

- Effect of reduction temperature (200 °C to 500 °C)
- Effect of heating rate during reduction (0.5 °C/min, 2.5 °C/min and 5 °C/min)
- Effect of moisture in reducing gas flow (20% $H_2$ in inert gas with/without $H_2O$)
- Effect of space velocity of reducing gas.

## 2 Experimental

### 2.1 Materials

Sodium tetrachloropalladate(II) hydrate (PdTC), chloroplatinic acid hydrate (CPA), tetraammine-palladium(II) chloride monohydrate (PdTA) and tetraammine-platinum(II) chloride hydrate (PTA) were used as Pd and Pt metal precursors. One high point of zero charge (PZC) carbon (Vulcan XC 72) and one low PZC carbon (Timrex HSAG300) were used as support. Silica (Aerosil 150) and alumina (VGL-25) were employed as oxide supports. HCl and NaOH were used to adjust pH of the metal stock solution. Table 1 gives a summary of the supports used and catalysts prepared. In a small

**Table 1** Summary of the supports and metals used, and the catalysts prepared

| Support | Pore volume (mL/gm) | PZC | Surface area ($m^2$/gm) | Catalysts prepared | | | |
|---|---|---|---|---|---|---|---|
| | | | | SEA Synthesized | | DI synthesized | |
| | | | | wt% Pt | wt.% Pd | wt.% Pt | wt.% Pd |
| Carbon HSAG300 'Timrex' | 0.7 | 4.5 | 280 | 1.6 (i)*<br>1.6 (e) | 1.3 (i)<br>1.3 (e) | 1.6 (i)*<br>5.6 (e) | 1.3 (i)<br>5.7 (e) |
| Carbon 'Vulcan XC 72' | 3.46 | 8.9 | 254 | 6.9 (i)<br>3.2 (e) | 2.5 (i)<br>2.5 (e) | 7.3 (i)<br>7.3 (e) | 2.5 (i)<br>4.5 (e) |
| $SiO_2$ 'Aerosil 150' | 1.25 | 3.7 | 130 | 2.2 (i)<br>2.2 (e) | 2.1 (i)<br>2.1 (e) | 2.0 (i)<br>2.0 (e) | 2.0 (i)<br>2.0 (e) |
| $\Upsilon$-$Al_2O_3$ 'VGL-25' | 1.7 | 8.5 | 277 | 8.6 (i)<br>4.0 (e) | 2.4 (i)<br>2.4 (e) | 7.1 (i)<br>7.1 (e) | 3.3 (i)<br>3.3 (e) |

*(i) – in-situ sample; (e) – ex-situ sample

number of cases, different metal loadings were used in the in-situ versus the ex-situ experiments, but in all cases SEA and DI preparations were compared at roughly the same loading.

## 2.2 Methods

Catalysts were prepared using two methods—strong electrostatic adsorption and dry impregnation. In SEA, metal precursor ions are adsorbed over oppositely charged support surfaces. This establishes a strong precursor-support interaction, which ultimately results in high metal dispersion with very small metal nanoparticle formation [4–9].

Over a high PZC support, electrostatic adsorption is achieved using anionic metal precursors over a protonated and positively charged surface at an optimal low pH of about 3. Over low PZC supports, cationic complexes are adsorbed over deprotonated and negatively charged support surfaces at an optimal pH of about 11. The pH of the room temperature precursor solution was adjusted using HCl or NaOH to initial pH values sufficient to give the optimal final pH values after contact with the support. The mass of the support in the solution was controlled to give a surface loading (SL) of 1500 $m^2$/L for all catalysts except for Pt on high PZC supports (VXC 72 and VGL-25) for which a second batch was prepared with 500 $m^2$/L to achieve higher weight loading of the metal. These higher Pt loaded samples (6.9% VXC72-CPA and 8.6% $Al_2O_3$-CPA) were used only for the in-situ XRD experiments.

After SEA impregnation, the solution containing the support was placed on an orbital shaker for 1 h at 140 rpm. The metal impregnated supports were recovered using vacuum filtration, removed to dry at 45 °C for 16 h and then reduced at various temperatures.

In dry impregnation the pore volume of the support material is filled with just enough amount of metal stock solution. In this case a strong metal precursor-support interaction is not guaranteed [2] and typically particle sizes are larger than what can be achieved by SEA. For DI synthesis we used appropriate concentrations of metal stock solution, added dropwise to the support until incipient wetness. The resulting paste was dried at 45 °C for 16 h before reduction. In cases where two weight loadings of metal were prepared, the lower weight loading was used for in-situ XRD experiments.

## 2.3 Catalyst Characterization

PerkinElmer Optima 2000 DV Inductively Coupled Plasma (ICP) was used to determine metal concentration in stock solution. Precursor solution samples before and after contact with the support are analyzed to find the difference in metal concentration which would be the amount of metal adsorbed by the support during SEA catalyst synthesis.

Reduced samples were examined by XRD in a Siemens D5000 diffractometer with CuKα radiation (λ = 1.5406 Å) operated at 30 kV and 40 mA, operating in Bragg–Brentano geometry. The angle range was set from 10 °C to 70° 2θ with a step size of 0.02° and 1.2 s exposure time at each angle. In-situ XRD experiments were performed in a Rigaku SmartLab SE X-ray diffractometer equipped with a D/tex Ultra250 1D silicon strip detector, with CuKα radiation (λ = 1.5406 Å) operated at 30 kV and 40 mA. An infrared heating system is used to enable precise temperature control. The angle range was set from 10 °C to 90° 2θ with a step size of 0.02° and scan speed 5 deg/min. Average crystallite sizes were calculated using the Scherrer equation with a K value of 0.94 with the Pt(111) peak at 39.8°2θ. Average crystallite sizes can be taken equal to average particle sizes when the nanoparticles are non-aggregated, as 1–6 nm particles are too small to be multi-grained. (This was consistent with TEM characterization.) Some samples reduced in humid environments did agglomerate appreciably and, in these cases, the aggregation of small crystallites into large "agglomerates" is discussed.

For ex-situ reduction experiments, samples were brought up to final temperatures of 200 °C, where they stayed for 1 h.

The samples were heated from room temperature at heating rates of 0.5 °C/min, 2.5 °C/min and 5.0 °C/min under 37 ml/min of continuous $H_2$ flow. Humidity and space velocity tests were done with 0.5 °C/min heating rate and 200 °C reduction temperature. In DI samples, we added 75 and 150 ml/min helium flow (noted as '75 He' and '150 He' in figures) to the reducing gas stream to reduce the vapor pressure of nascent, evolving water to moderate and higher degrees. On the other hand, humidity was increased by introducing 0.76 mg/min $H_2O$ into the 37 ml/min $H_2$ gas stream via a room temperature bubbler; this condition is noted as 'water'.

With SEA samples, besides the room temperature humidification ('water'), a lower degree of humidification was employed by passing the reducing gas through a water bath at 3 °C (resulting in 0.22 mg/min $H_2O$). This condition is denoted 'ice' in figures. An outline of the ex-situ experiments is shown in Fig. 1.

The steps and parameters used for in-situ XRD measurements are shown in Fig. 2. Each sample was placed in flowing $N_2$ at 100 sccm, dried at 120 °C for one hour, and cooled to 30 °C. Thereafter, 20 sccm of nitrogen was replaced by hydrogen, and after an initial XRD at 30 °C, additional scans were made at 100 °C intervals from 200 to 500 °C. A final scan was made when the sample cooled to room temperature. The heating rate was 3 °C/min.

STEM Z-contrast image analysis for all catalyst samples was performed on a JEOL JEM-2010F TEM/STEM. It is a 200 kV field emission transmission electron microscope with a Schottky field emission electron source and fitted with an ultra-high resolution pole piece. A probe size of 0.13 nm for DI samples, and 0.078 nm for SEA samples, with 15 pA of current was used. Images were taken using a high angle annular dark field detector. Each image was then analyzed by counting 500–1000 particles using "Particle2.exe" software to determine average particle size. Histograms for each sample are given in the supplementary information.

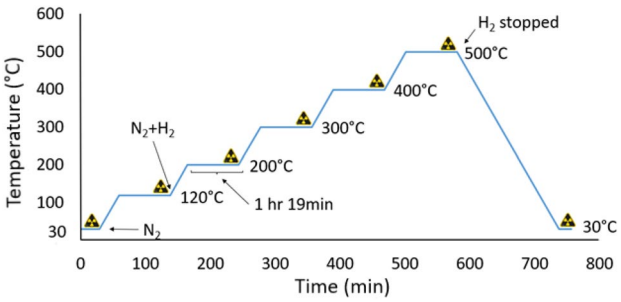


**Fig. 2** In-situ XRD steps and parameters

## 3 Results and Discussion

### 3.1 1: In-Situ XRD

In-situ XRD was employed to investigate the effect of reduction temperature in a flowing mixture of 20% $H_2$ in $N_2$ at 100 sccm on SEA and DI-derived samples. An initial check of the support materials showed their XRD patterns to be independent of the reduction temperature after reductions up to 500 °C (Fig. S1). Mass spectrum analysis of VXC72 and VXC72-PdTC-SEA confirmed there is no methanation of carbon in the investigated temperature range (Fig. S2),

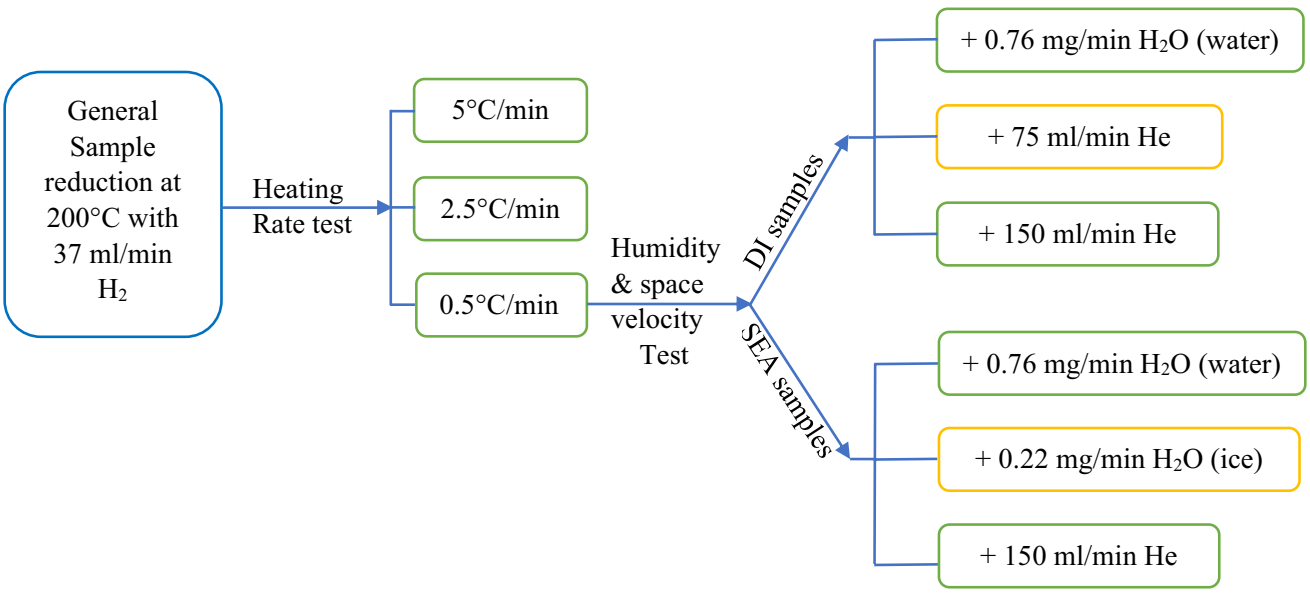


**Fig. 1** Outline of ex-situ experiments

and BET surface analysis of VXC72-PdTC-SEA showed no significant surface area and pore volume change between catalyst reduced at 200 °C (152 $m^2$/gm and 0.222 $cm^3$/gm) and 500 °C (161 $m^2$/gm and 0.226 $cm^3$/gm), indicating that supports remain stable during the experiments.

XRD patterns of the Pt series of materials are given in Fig. 3. The two carbon supports are shown in Fig. 3a, b; over the low PZC Timrex carbon (Fig. 3a), cationic Pt tetraammine was used for the SEA synthesis while over the high PZC Vulcan carbon (Fig. 3b), anionic Pt hexachloride was employed. For neither SEA-derived series do Pt peaks appear as the reduction temperature is increased through 500 °C. The limit of detection of this high sensitivity detector is about 1 nm [18, 19]. On the other hand,

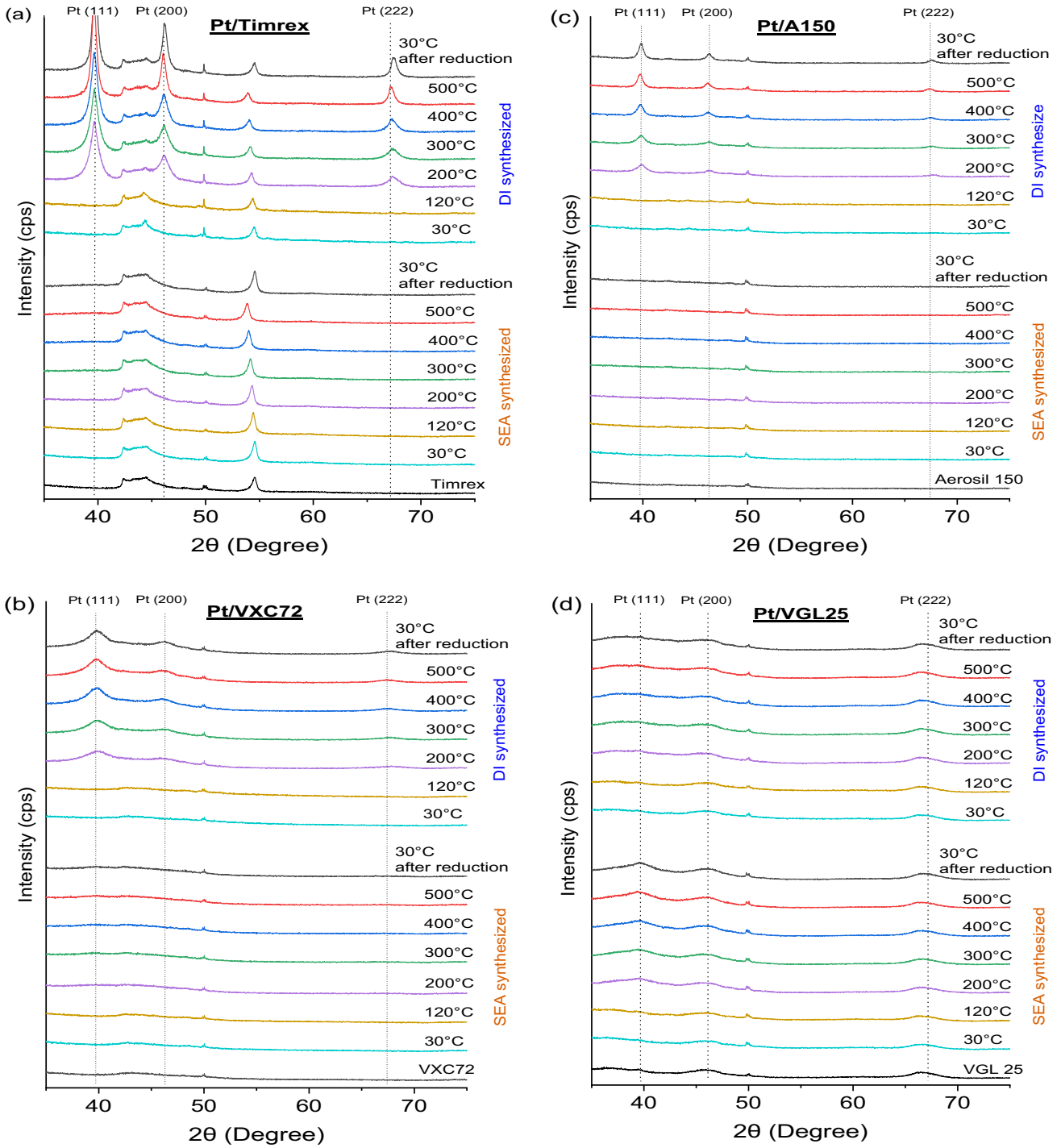


**Fig. 3** XRD patterns of Pt on different supports with changing temperature

DI preparations using the same precursors feature Pt peaks which sharpen with increasing reduction temperature. Over Timrex (Fig. 3a) DI-derived nanoparticles measured to be 6.5 nm at 200 °C in hydrogen grow to 10.7 nm at 500 °C. Over VXC 72, 1.7 nm particles observed at 200 °C grow to 2.3 nm at 500 °C. Particles sizes for all the in-situ XRD experiments are summarized in Fig. 5.

Results of the Pt/silica and Pt/alumina samples are shown in Fig. 3c, d. Like the low PZC carbon, cationic Pt tetraammine was employed for SEA over (low PZC) silica and these samples show no growth of crystallinity for reduction temperature up to 500 °C (Fig. 3c). As with the low PZC carbon, DI synthesized samples on silica show significant crystallinity, growing from 6 nm at 200 °C to 10.5 nm at 500 °C. And while the SEA Pt/alumina samples in Fig. 3d show no significant crystallinity up to 500 °C, neither do the DI-prepared samples. This stems from the precursor employed, chloroplatinic acid. The protons dissociated from the chloroplatinic acid can charge the alumina surface and induce electrostatic adsorption at incipient wetness; this process has been termed "charge-enhanced dry impregnation" (CEDI) and has been demonstrated previously with cationic Pt adsorbing over a negatively charged silica surface [20]. Here, anionic Pt is adsorbing over a protonated and positively charged alumina surface at incipient wetness. Using a nonacidic Pt hexachloride salt such as $K_2PtCl_6$ with DI results in typically large Pt particles [21].

Results for Pd preparations over the high PZC carbon and alumina and low PZC carbon and silica supports are shown in Fig. 4. Pd over Timrex (Fig. 4a) behaves similarly to Pt over Timrex (Fig. 3a); no peaks are observed for the SEA-derived samples through reductions up to 500 °C while DI samples show appreciable crystallinity from 200 °C. Over VXC72 (Fig. 4b), SEA-derived particles sizes are smaller than DI-derived particles at any one reduction temperature, but in this case, small metallic Pd peaks are seen in the dried sample at 30 °C. This is evidence of a parallel deposition mechanism, which has been postulated during SEA of Pt at long contact times [8] but in this case appears to happen more rapidly for Pd. The integrated intensity of the crystalline Pd peaks is lower for the SEA-derived samples than for the DI-derived samples, implying that a substantial fraction of the SEA-derived Pd nanoparticles is below the limit of detection. Finally, upon exposure to room conditions after the reduction, the DI sample on VXC72 also displayed the most intense peak of PdO.

Similar to the Pt/silica sample (Fig. 3c), the SEA-derived Pd/silica (Fig. 4c) shows no crystallinity at reductions up to 500 °C, while DI-derived samples show particles of 12.7 nm at 200 °C sintering further to 18.9 nm at 500 °C. Curiously, for Pd on alumina (Fig. 4d), both the DI and SEA syntheses show insignificant crystallinity through reductions of 500 °C. In fact, the Pd precursor had acid impurity which reduced the stock solution pH to ~ 4 at the high concentration needed for DI synthesis and seems to have induced charge on the alumina surface that mimicked SEA to some extent and resulted in small particles.

Particle sizes estimated from the in-situ XRD runs are summarized in Fig. 5. Size estimates for samples in which only part of the metal is observable were obtained by approximating the fraction of observable metal by comparison with a large-particle standard, and attributing the fraction of metal below the detection limit a size of 1 nm (see Supplementary Information). For Pt (Fig. 5a), all SEA synthesized particles are very stable through 500 °C (~ 1 nm). DI synthesized Pt/Timrex and $Pt/SiO_2$ gives large particle size which increases with increasing reduction temperature. The small particle size of DI-synthesized Pt on VXC72 is due to the CEDI phenomenon. Particles are also small and comparatively stable for Pt/alumina samples for the same reason.

For Pd (Fig. 5b), Pd SEA on Timrex, silica, and alumina produced small nanoparticles which were stable during the heat treatment, while SEA on VXC72 was accompanied by another deposition mechanism which allowed larger particles to form. Among DI synthesized Pd samples, Pd on $SiO_2$ gave largest particles that sintered significantly with increasing temperature. Pd/Timrex samples yielded approximately 6 nm particles through a reduction temperature of 500 °C. DI-derived Pd/VXC72 particles increased from 2.5 nm to 3.7 nm from 200 to 500 °C. As mentioned above, $Pd/Al_2O_3$ also yielded undetectable particles through 500 °C.

### 3.2 3.2 Ex-Situ Experiments

In addition to studying the effect of reduction temperature with in-situ XRD, additional experiments for each of the eight systems (Pt and Pd over low PZC carbon, high PZC carbon, silica, and alumina) were conducted via ex-situ XRD and STEM to observe the effect of heating ramp rate (0.5, 2.5, and 5 °C/min) and water vapor pressure in the reducing gas as controlled by space velocity and direct water addition. In the former adjustment, higher gas flow rates should minimize the vapor pressure of nascent water produced during the reduction process.

A summary of particle sizes with changing heating rate is given in Fig. 6, for DI (Fig. 6a) and SEA (Fig. 6b) prepared materials. The larger average size of the DI samples versus SEA samples is immediately noticeable, and the particle sizes fluctuate more than the SEA samples by the influence of heating ramp rate. The smallest DI samples were the chloroplatinic acid on alumina and VXC-72 samples, due to the partial charging of the support surfaces. The SEA samples' particle sizes remain comparatively independent of heating rate with Pd showing a small amount of variability.

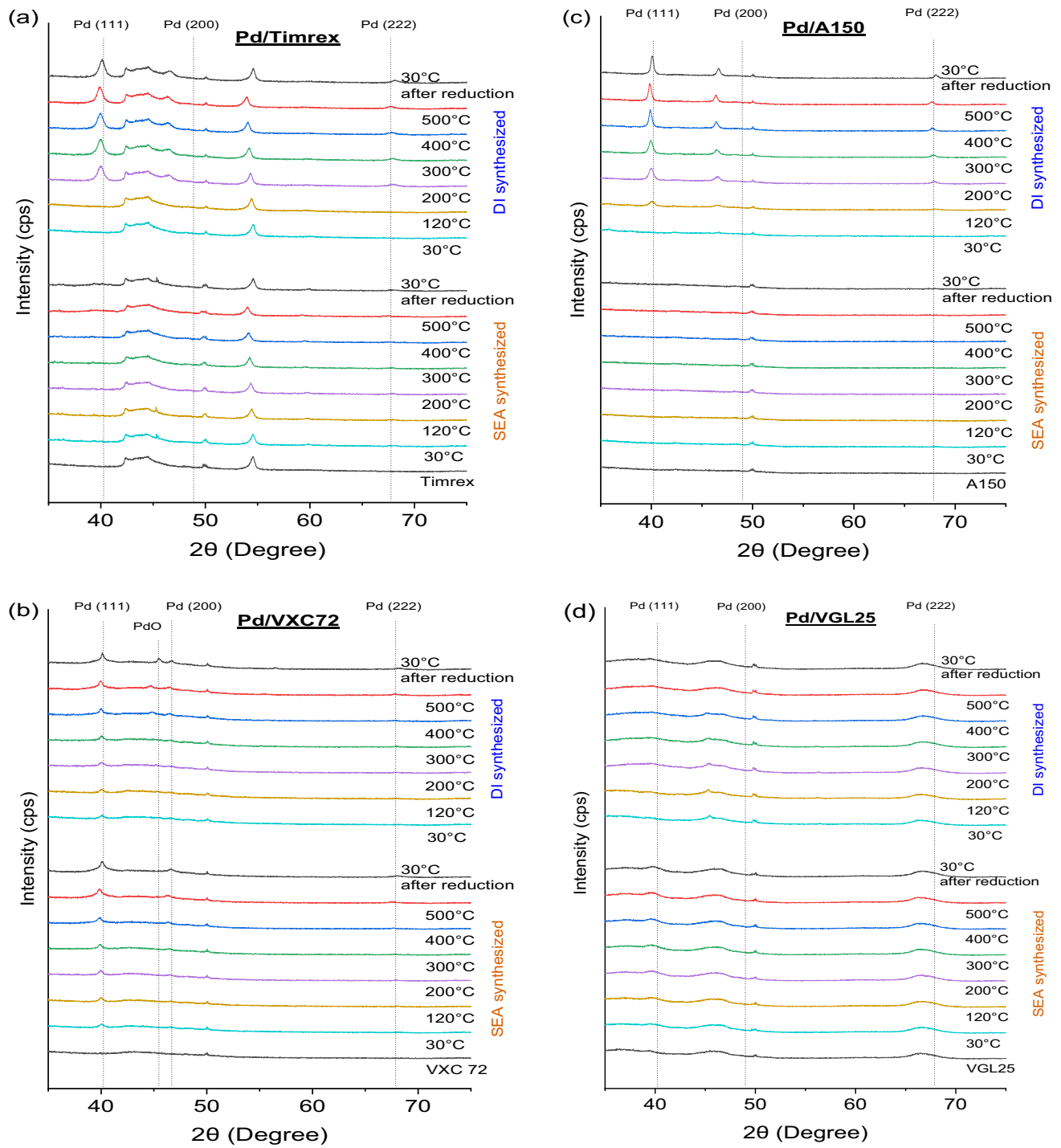


**Fig. 4** XRD patterns of Pd on different supports with changing temperature

The detailed results for heating rate and water exposure are best conveyed by a comparison of STEM results of the DI and SEA samples. Those results for Pt/Timrex are shown in Fig. 7 for the heating rate experiments (Fig. 7a, b, top row) and the water vapor pressure results (Fig. 7a, b, bottom row). Histograms for these STEM images are given in Fig. S3. The DI particles are relatively large and show some variation in size versus heating rate, while the size of the SEA-derived particles is virtually constant. While the DI samples show a small increase in particle size with increasing space velocity (Fig. 6a, bottom row) via STEM, the DI XRD (Fig. 7c) of the higher space velocity sample, which

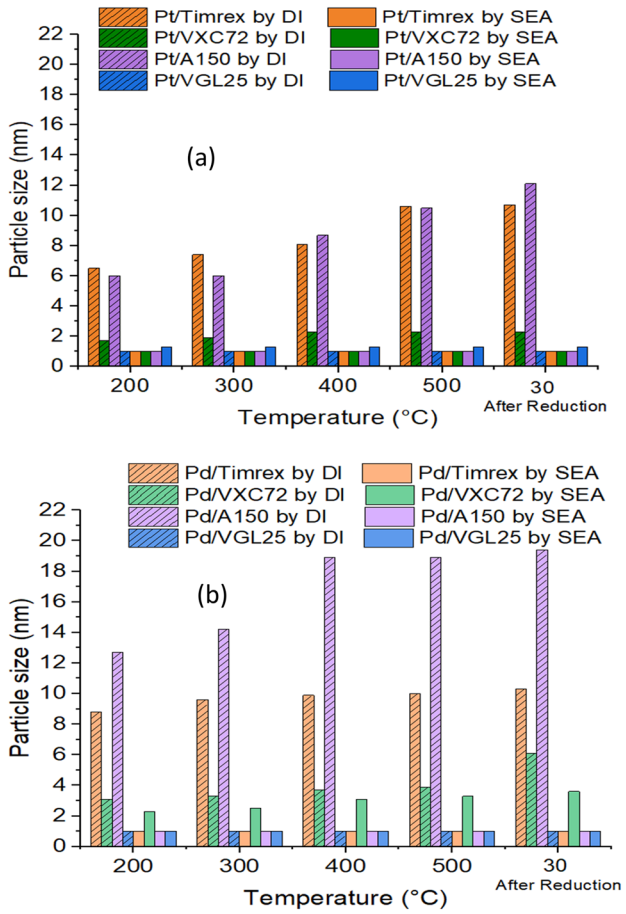


**Fig. 5** All (**a**) Pt and (**b**) Pd particle size based on in-situ XRD

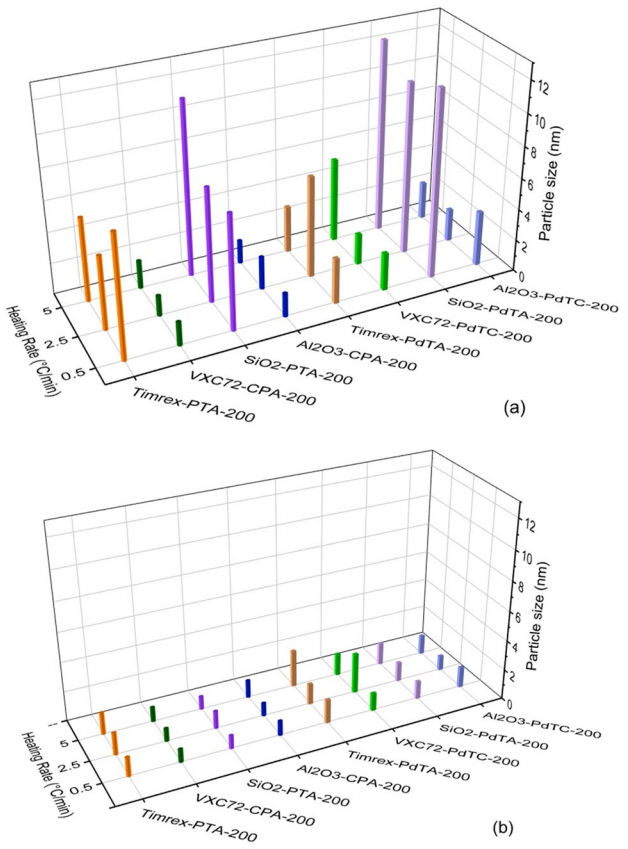


**Fig. 6** The effect of heating rate on particle size on (**a**) DI and (**b**) SEA prepared samples

is likely more representative of the bulk, shows a slight decrease. When water is added via a room temperature bubbler, STEM reveals a dramatic coalescence of particles even while the XRD patterns of the of the sample shows only a slight increase in size. The large aggregates seen in the STEM image of the wet-reduced DI sample must then result from a coalescence of the approximately 6 nm particles. The size of the SEA-derived nanoparticles, on the other hand, is not affected by the heating rate (Fig. 6b, top row) and more significantly, the SEA-derived nanoparticles show only a slight sintering and no coalescence with the room temperature-wetted hydrogen stream.

The behavior of the Pt/VXC-72 samples is similar to Pt/Timrex; STEM and XRD patterns for this sample are shown in Fig. 8 and STEM histograms in Fig. S4. The DI particles in this sample were smaller from the CEDI effect. They show some growth at the higher heating rate, and extensive coalescence in humid hydrogen (Fig. 8a). On the other hand, the SEA sample size is nonvariant with heating rate, and shows some sintering but no coalescence in humid reducing conditions (Fig. 8b). The XRD patterns of the room temperature water-reduced DI and SEA samples are about the same (Fig. 8c) which again signals that the aggregates in the DI sample are coalesced smaller particles.

Results for the Pt/silica samples are shown in Fig. 9, with the STEM histograms given in Fig. S5. The DI samples are all more aggregated than either of the carbon supported samples and the heating rate runs showed some variability, yet in the humidified reduction, extensive coalescence was again observed (Fig. 9a, bottom row). XRD of the DI samples (Fig. 9c) confirms that the large clusters are aggregates of the 6–7 nm nanoparticles. The behavior of the SEA samples is again similar to the carbon supported samples (Fig. 9b); size is unaffected by heating rate, and the humid reductions caused some sintering but no coalescence.

Finally, the results for the Pt/alumina samples shown in Fig. 10 (histograms in Fig. S6) are quite consistent with those over Pt/VXC72. Once again, the CEDI effect yields smaller sizes for the DI samples and less sensitivity to the heating rate (Fig. 10a) versus the non-CEDI silica and Timrex DI samples (Figs. 7a and 9a). The humid hydrogen sample again shows extreme coalescence of particles which XRD shows to be about 9 nm (Fig. 10c). The SEA samples show invariability to heating rate and higher stability to humid reductions, including a slight sintering but no

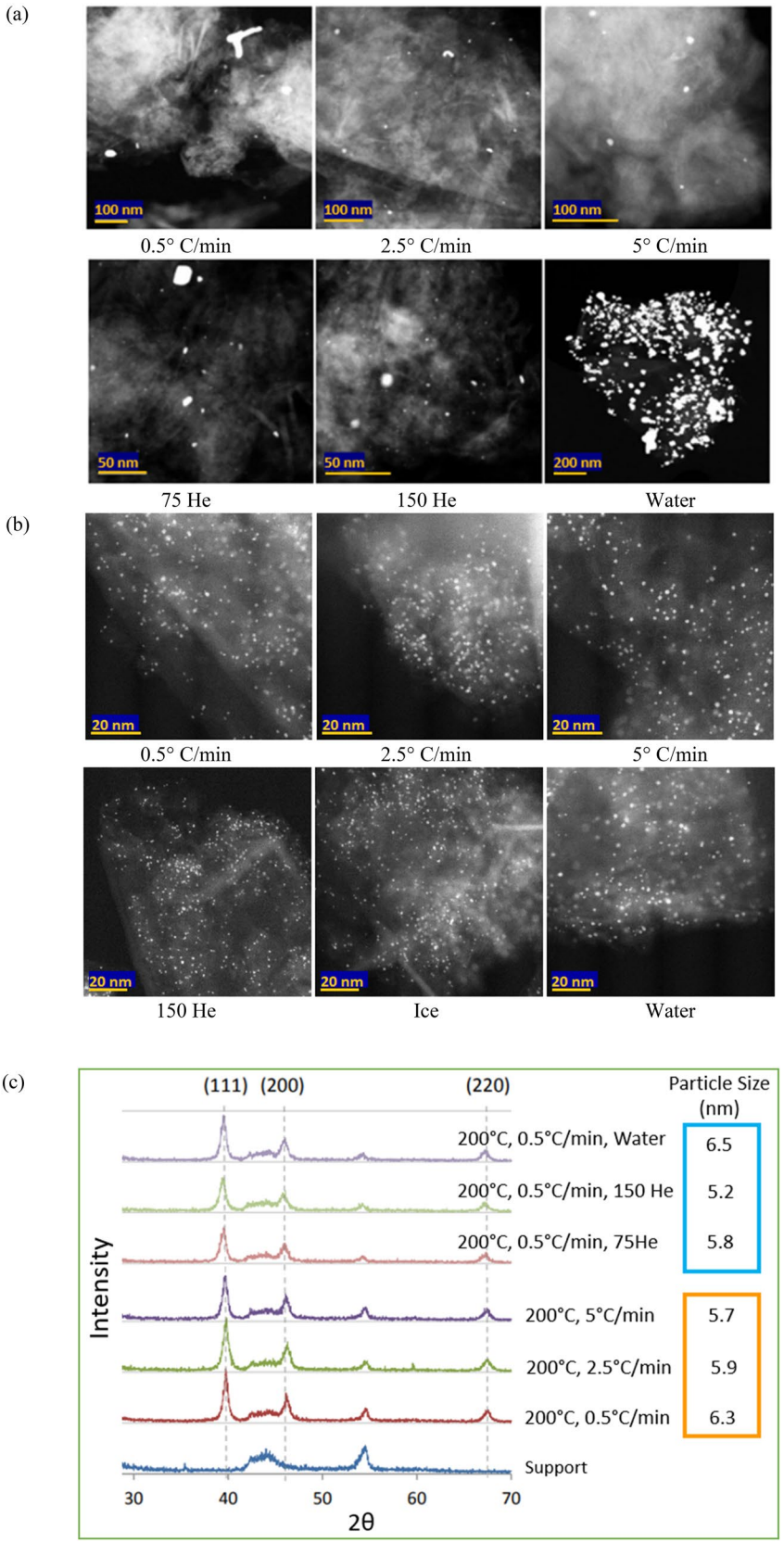


**Fig. 7** STEM images of Pt/Timrex (**a**) DI, (**b**) SEA; and (**c**) XRD patterns of the DI samples—showing the effect of heating rate and moisture

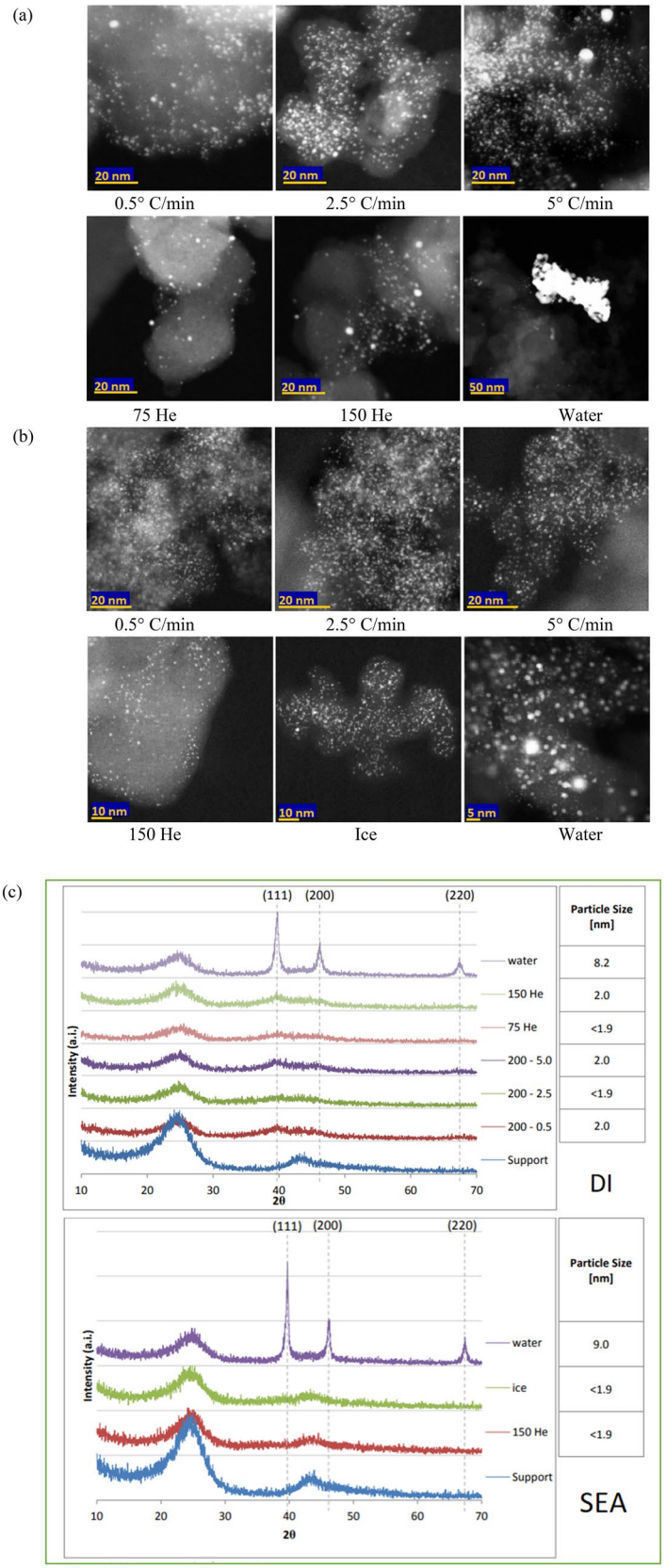


**Fig. 8** STEM images of Pt/VXC72 (**a**) DI, (**b**) SEA; and (**c**) XRD patterns—showing the effect of heating rate and moisture

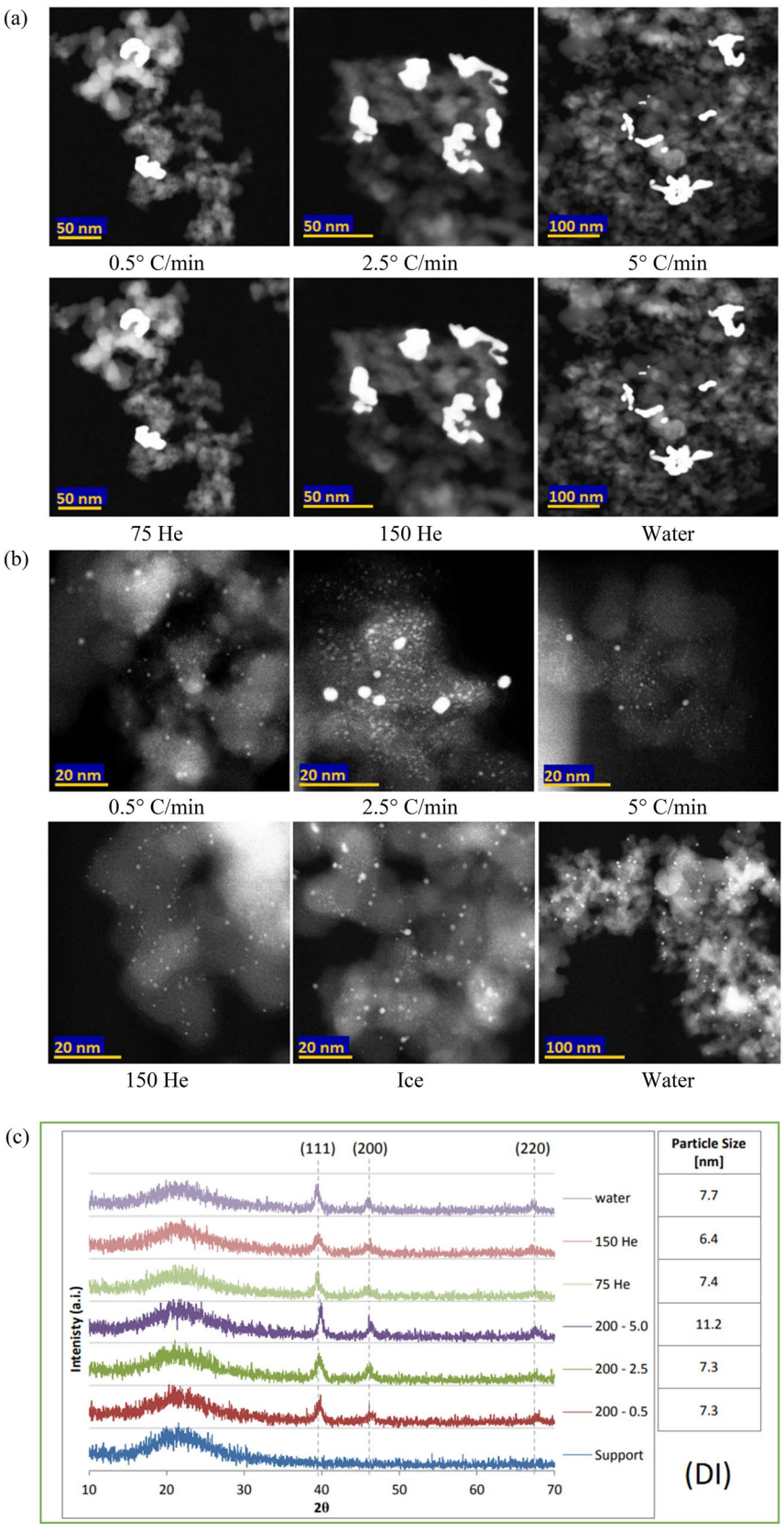


**Fig. 9** STEM images of $Pt/SiO_2$ (**a**) DI, (**b**) SEA; and (**c**) XRD patterns—showing the effect of heating rate and moisture

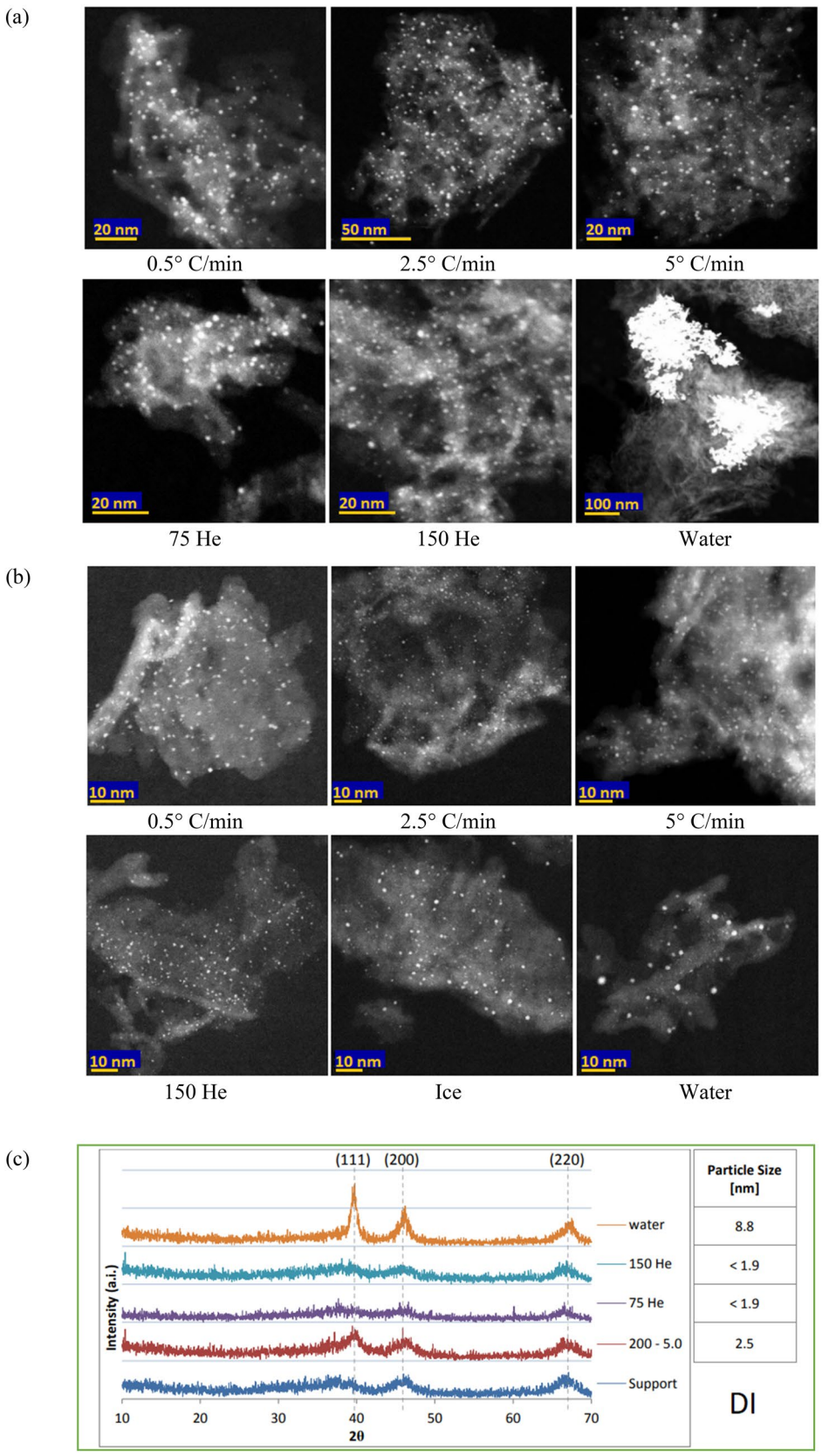


**Fig. 10** STEM images of Pt/$Al_2O_3$ (**a**) DI, (**b**) SEA; and (**c**) XRD patterns—showing the effect of heating rate and moisture

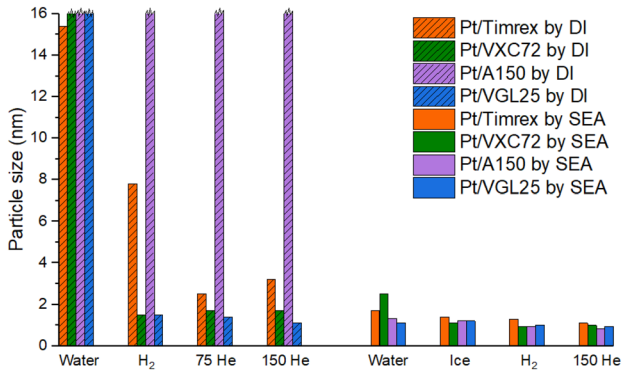


**Fig. 11** Effect of water partial pressure in reducing gas on Pt particle size

coalescence in the highest humidity reduction environment (Fig. 10b).

A summary comparison of STEM particle sizes for the DI and SEA samples in flows containing controlled humidity is shown in Fig. 11. Results are ordered with respect to degree of humidification, with the most humid on the left and least humid on the right. The "$H_2$" label refers to the standard flowing hydrogen stream. The stability of the SEA vis-à-vis DI samples for all four supports is clearly seen. In addition, the small particle size and relative stability in humid reductions of DI preparations on the high PZC supports, VXC72 and alumina, for which chloroplatinic acid induces some degree of electrostatic adsorption, is also evident. Water clearly catalyzes nanoparticle coalescence.

Only the heating rates were explored for the Pd-containing samples. These are seen in the right side of Fig. 6 and with a bit more variability in the carbon-supported samples, largely parallel the Pt samples. The STEM, histogram, and XRD data for these samples are given in the supplementary information in Figs. S7–10.

To this point it has been demonstrated empirically that the SEA-derived samples are relatively small in size and insensitive to not only reduction heating rate, but also final reduction temperature and are less prone to coalesce during humid reductions versus DI-prepared samples, especially the DI preparations completely free of electrostatic interactions. The question which remains is why.

In the first place, it is known that supported nanoparticles with monodisperse size distributions are more stable to sintering than polydispersed particles [22, 23]; if all nanoparticles are the same size there is no driving force for sintering. This explains in general the higher stability toward sintering at high temperatures and in high humidity of the SEA-derived nanoparticles versus the CEDI-derived nanoparticles versus the DI-derived nanoparticles.

The histograms of the DI samples which have significantly sintered at higher reduction temperatures in Figs. S3–7 have a log normal distribution indicating extensive particle growth. However, it has been shown for supported catalysts that a right-hand skew of the particle size distribution does not prove the particle sintering and coalescence mechanism, nor rule out Ostwald ripening [24]. The most convincing mechanistic information is that for the highly aggregated images seen in STEM of the DI-derived, humid-reduced samples in Figs. 7, 8, 9 and 10. These aggregates are comprised of smaller particles as shown by XRD, confirming that coalescence occurs in all DI samples, even in the case of the charge enhanced systems of the high PZC carbon (VXC72) and alumina supports. The relative stability of the SEA-derived samples in the same humid environment is remarkable.

In a final comment, the size of the SEA-derived nanoparticles does not increase with increasing reduction temperature, and the nature of this stability can be speculated in light of the scenarios schematized in Fig. 12. If the initial deposition of electrostatically adsorbed precursors is uniform as illustrated in Fig. 12a, it would be expected that higher reduction temperatures would lead to more precursor migration and larger particle size. If, however, during the drying process, the precursors aggregate into nanodroplets of water as the drying occurs, which is to say that surface tension replaces electrostatic attraction as the local environment changes from aqueous to gaseous, then deposited aggregates will form same-sized nanoparticles which resist migration at higher reduction temperature. Work on this aspect of supported nanoparticle synthesis is ongoing.

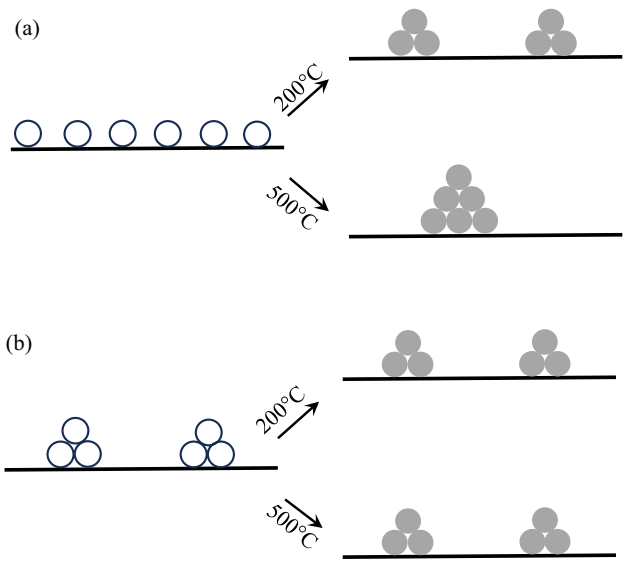


**Fig. 12** Schematic of initial precursor distribution after SEA, (**a**) uniform, (**b**) aggregated

## 4 Conclusion

The effect of reduction pretreatments on final particle size has been conducted using in-situ and ex-situ XRD and STEM over a series of carbon and oxide supported Pt and Pd nanoparticles prepared by strong electrostatic adsorption and dry impregnation. The DI samples show in general the expected increase in size with reduction temperature, some variability in size with the reduction heating rate, and extreme coalescence in a humid reducing environment. On the other hand, the SEA-derived nanoparticles with much generally much smaller initial nanoparticle size and a much more uniform particle size distribution, show (with a few minor exceptions for Pd) no increase in size with reduction temperature, are not affected by the heating rate, and are remarkably stable in a humid reducing environment, showing only small amounts of sintering but no particle coalescence. The difference in behavior is believed to stem from the uniformity of the SEA-derived particle size. The absence particle growth at higher reduction temperatures of SEA-deposited precursors is suggested to arise from a small-scale aggregation of the precursors during drying.

**Supplementary Information** The online version contains supplementary material available at https://doi.org/10.1007/s10562-024-04640-y.

**Funding** Open access funding provided by the Carolinas Consortium.



## References

1. Niemantsverdriet JW (2007) Spectroscopy in catalysis an introduction. Wiley-VCH, Weinheim
2. Regalbuto J (ed) (2006) Catalyst preparation: science and engineering, 1st edn. CRC Press, Boca Raton. https://doi.org/10.1201/9781420006506
3. Burkholder MB, Rahman MM, Reber AC, Gaffney AM, Gupton BF, Monnier JR (2023) New perspectives and insights into direct epoxidation of propylene using $O_2$ and silver-based catalysts. Appl Catal A Gen 650:119002. https://doi.org/10.1016/J.APCATA.2022.119002
4. Jiao L, Regalbuto JR (2008) The synthesis of highly dispersed noble and base metals on silica via strong electrostatic adsorption: I. Amorphous silica. J Catal 260(2):329–341. https://doi.org/10.1016/J.JCAT.2008.09.022
5. Regalbuto J (ed) (2016) Catalyst preparation. CRC Press. https://doi.org/10.1201/9781420006506
6. Samad JE, Keels J, Regalbuto JR (2016) A comparison of Pt(II) and Pt(IV) chloride precursors for strong electrostatic adsorption synthesis of Pt/alumina and Pt/carbon catalysts. Catal Lett 146(1):157–162. https://doi.org/10.1007/s10562-015-1631-3
7. Seuser GS et al (2018) Understanding uptake of Pt precursors during strong electrostatic adsorption on single-crystal carbon surfaces. Top Catal 61(5–6):379–388. https://doi.org/10.1007/s11244-017-0872-3
8. Hao X, Barnes S, Regalbuto JR (2011) A fundamental study of Pt impregnation of carbon: adsorption equilibrium and particle synthesis. J Catal 279(1):48–65. https://doi.org/10.1016/j.jcat.2010.12.021
9. Lambert S et al (2009) Synthesis of very highly dispersed platinum catalysts supported on carbon xerogels by the strong electrostatic adsorption method. J Catal 261(1):23–33. https://doi.org/10.1016/j.jcat.2008.10.014
10. Mehrabadi BAT, Eskandari S, Khan U, White RD, Regalbuto JR (2017) A review of preparation methods for supported metal catalysts 1–35. https://doi.org/10.1016/bs.acat.2017.10.001
11. de Jong KP (ed) (2009) Synthesis of solid catalysts. Wiley. https://doi.org/10.1002/9783527626854
12. Kim K-J et al (2010) Effect of pretreatment conditions on particle size of bimetallic Pt–Au catalysts supported on ZnO/$Al_2O_3$ and its activity for toluene oxidation. J Nanosci Nanotechnol 10(9):5869–5873. https://doi.org/10.1166/jnn.2010.3085
13. Liu CH, Lin CY, Chen JL, Lu KT, Lee JF, Chen JM (2017) SBA-15-supported Pd catalysts: the effect of pretreatment conditions on particle size and its application to benzyl alcohol oxidation. J Catal 350:21–29. https://doi.org/10.1016/j.jcat.2017.01.019
14. Gao X, Ashok J, Kawi S (2022) A review on roles of pretreatment atmospheres for the preparation of efficient Ni-based catalysts. Catal Today 397–399:581–591. https://doi.org/10.1016/j.cattod.2021.06.009
15. van de Loosdrecht J et al (2003) Calcination of Co-based Fischer-Tropsch synthesis catalysts. Top Catal 26:121–127
16. Garetto TF, Apesteguía CR, Le Normand F, Moraweck B, Borgna A (1999) Sintering of chlorinated Pt/γ -$Al_2O_3$ catalysts: an in situ study by X-Ray absorption spectroscopy. J Catal 186:433–441
17. Radivojević D, Seshan K, Lefferts L (2006) Preparation of well-dispersed Pt/$SiO_2$ catalysts using low-temperature treatments. Appl Catal A Gen 301(1):51–58. https://doi.org/10.1016/j.apcata.2005.11.016
18. Taguchi T (2006) A new position sensitive area detector for high-speed and high-sensitivity X-ray diffraction analysis. Powder Diffr 21(2):97–101. https://doi.org/10.1154/1.2204063
19. O'Connell K, Regalbuto JR (2015) High sensitivity silicon slit detectors for 1 nm powder XRD size detection limit. Catal Letters 145(3):777–783. https://doi.org/10.1007/s10562-015-1479-6
20. Zhu X, Cho H, Pasupong M, Regalbuto JR (2013) Charge-enhanced dry impregnation: a simple way to improve the preparation of supported metal catalysts. ACS Catal 3(4):625–630. https://doi.org/10.1021/cs3008347
21. Liu J, Regalbuto JR (2012) Molecular characterization of noble metal adsorption at the water-aluminum oxide interface. Adv Chem Eng 396–398:745
22. Liang C et al (2022) Sintering behaviors of supported nanoparticles related to spatial location by a quasi-four-dimensional TEM. Nano Lett 22(16):6523–6529. https://doi.org/10.1021/acs.nanolett.2c01538
23. Dai Y, Lu P, Cao Z, Campbell CT, Xia Y (2018) The physical chemistry and materials science behind sinter-resistant catalysts. Chem Soc Rev 47(12):4314–4331. https://doi.org/10.1039/C7CS00650K

24. Datye AK, Xu Q, Kharas KC, McCarty JM (2006) Particle size distributions in heterogeneous catalysts: what do they tell us about the sintering mechanism? Catal Today 111(1–2):59–67. https://doi.org/10.1016/j.cattod.2005.10.013



## Authors and Affiliations

**Md. Fakhruddin Patwary[1] · Manuel Neito[2] · Alaba Ojo[1] · John R. Regalbuto[1]**

✉ John R. Regalbuto
regalbuj@cec.sc.edu

[1] Department, of Chemical Engineering, University of South Carolina, Columbia, SC, USA

[2] Department of Chemical Engineering, University of Illinois at Chicago, Chicago, IL, USA